# Ocean Surface Gravity Wave Excitation of Flexural Gravity and Extensional Lamb Waves in Ice Shelves

**L.S. Abrahams** * [1], **J.E. Mierzejewski** [2], **E.M. Dunham** [1,3]

[1]Department of Geophysics, Stanford University, Stanford, CA, USA, [2]California State University, Los Angeles, [3]Institute of Computational and Mathematical Engineering, Stanford University, Stanford, CA, USA

Author contributions: *Conceptualization*: L.S. Abrahams, E.M. Dunham. *Software*: L.S. Abrahams, E.M. Dunham. *Validation*: L.S. Abrahams, E.M. Dunham. *Formal Analysis*: L.S. Abrahams, E.M. Dunham. *Investigation*: L.S. Abrahams, J.E. Mierzejewski, E.M. Dunham. *Writing - original draft*: L.S. Abrahams, E.M. Dunham. *Writing - Review & Editing*: L.S. Abrahams, J.E. Mierzejewski, E.M. Dunham. *Visualization*: L.S. Abrahams, J.E. Mierzejewski. *Supervision*: L.S. Abrahams, E.M. Dunham. *Project administration*: E.M. Dunham. *Funding acquisition*: L.S. Abrahams, E.M. Dunham.

This manuscript is a non-peer reviewed preprint submitted to EarthArXiv. It is currently in review with Seismica.

*Corresponding author: labraha2@stanford.edu

# Ocean Surface Gravity Wave Excitation of Flexural Gravity and Extensional Lamb Waves in Ice Shelves

**L.S. Abrahams** * [1], **J.E. Mierzejewski** [2], **E.M. Dunham** [1,3]

[1]Department of Geophysics, Stanford University, Stanford, CA, USA, [2]California State University, Los Angeles, [3]Institute of Computational and Mathematical Engineering, Stanford University, Stanford, CA, USA

Author contributions: *Conceptualization*: L.S. Abrahams, E.M. Dunham. *Software*: L.S. Abrahams, E.M. Dunham. *Validation*: L.S. Abrahams, E.M. Dunham. *Formal Analysis*: L.S. Abrahams, E.M. Dunham. *Investigation*: L.S. Abrahams, J.E. Mierzejewski, E.M. Dunham. *Writing - original draft*: L.S. Abrahams, E.M. Dunham. *Writing - Review & Editing*: L.S. Abrahams, J.E. Mierzejewski, E.M. Dunham. *Visualization*: L.S. Abrahams, J.E. Mierzejewski. *Supervision*: L.S. Abrahams, E.M. Dunham. *Project administration*: E.M. Dunham. *Funding acquisition*: L.S. Abrahams, E.M. Dunham.

**Abstract** Flexure and extension of ice shelves in response to incident ocean surface gravity waves have been linked to iceberg calving, rift growth, and even disintegration of ice shelves. Most modeling studies utilize a plate bending model for the ice, focusing exclusively on flexural gravity waves. Ross Ice shelf seismic data shows not only flexural gravity waves, with dominantly vertical displacements, but also extensional Lamb waves, which propagate much faster with dominantly horizontal displacements. Our objective is to model the full-wave response of ice shelves, including ocean compressibility, ice elasticity, and gravity. Our model is a 2D vertical cross-section of the ice shelf and sub-shelf ocean cavity. We quantify the frequency-dependent excitation of flexural gravity and extensional Lamb waves and provide a quantitative theory for extensional Lamb wave generation by the horizontal force imparted by pressure changes on the vertical ice shelf edge exerted by gravity waves. Our model predicts a horizontal to vertical displacement ratio that increases with decreasing frequency, with ratio equal to unity at $\sim$0.001 Hz. Furthermore, in the very long period band ($< 0.003$ Hz), tilt from flexural gravity waves provides an order of magnitude larger contribution to seismometer horizontal components than horizontal displacements from extensional Lamb waves.

**Non-technical summary** In the past three decades, we have seen ice shelves catastrophically weaken and break apart. In some cases, large calving events or ice shelf disintegration is correlated to the arrival of ocean waves and tsunamis. This has prompted the deployment of seismometers on ice shelves to study the ice shelf response to ocean wave impacts. Ocean waves convert to several other wave modes in the ice shelf and ocean layer beneath the ice shelf. In our study, we present computer simulations of the ocean and ice shelf system to quantify the wave motions within and on the surface of the ice shelf, thereby permitting comparison to seismic data. Our results help guide interpretation of seismic data and in understanding which wave modes are most likely to contribute to calving and fracture of ice shelves.

## 1 Introduction

Ice shelf stability and strength play an important role in understanding and predicting sea level rise (Bromwich and Nicolas, 2010). Ice shelves buttress ice sheets and following ice shelf collapse, ice streams have been observed to accelerate (Dupont and Alley, 2005; Pritchard et al., 2012). In the past three decades, we have seen ice shelves catastrophically weaken and break apart; as the climate continues to warm, thinning and collapse of ice shelves is likely to occur at a more rapid rate.

Weakening of ice shelves has been associated with wave-induced flexure (Holdsworth and Glynn, 1978) as well as basal and surface melting (Paolo et al., 2015). Basal melting is facilitated through influx (into the sub-ice shelf cavity) of warm seasonal sea water and circumpolar deep water (Walker et al., 2008; Rignot et al., 2013). During the

*Corresponding author: labraha2@stanford.edu
*Corresponding author: labraha2@stanford.edu

summer months, surface melting increases, creating supraglacial lakes, further thinning the ice shelves and possibly contributing to hydro-fracturing into the ice shelf (Banwell et al., 2013).

Melting and thinning weaken ice shelves, but what creates fractures and finally triggers the collapse of ice shelves is poorly determined. Possible processes include ocean surface gravity wave forcing (Holdsworth and Glynn, 1978; Bromirski et al., 2010; Brunt et al., 2011; Banwell et al., 2017; Massom et al., 2018). Incident ocean waves are partially transmitted into the ice shelf as flexural gravity waves (similar to ocean surface gravity waves but with additional inertia and elastic resistance to bending from the ice) and other elastic waves bearing more similarity to traditional seismic waves. The ability of waves to transmit through the ice shelf and the magnitude of wave-induced stresses depend on the ice shelf structure (ice thickness, elastic moduli, density), depth of water in the sub-shelf cavity, and the properties of the incident wave (frequency, incident angle). Incident waves include high frequency ocean swells, storm-generated infragravity waves, tides, and tsunamis (MacAyeal et al., 2006). Lower frequency waves penetrate the sub-shelf cavities more efficiently, causing flexure (Sergienko, 2013). This flexural stress can open cracks, drive rift growth, and initiate collapse events. Bromirski et al. (2010) concluded that both of the breakup events on the Wilkins Ice shelf in 2008 matched with arrivals of infragravity waves from large storm events on the Patagonian coast. Brunt et al. (2011) suggested that tsunami arrivals from the 2011 Tohoku-Oki, Japan, earthquake caused a massive calving event on the Sulzberger Ice Shelf. Massom et al. (2018) linked storm-generated swell to calving and break-up of the Larsen A and B and Wilkins ice shelves. Icequake activity near the front of the Ross Ice Shelf is also correlated ocean wave arrivals (Chen et al., 2019; Aster et al., 2021), though other factors such as tidal and thermal stresses contribute as well (Olinger et al., 2019). Flexural gravity waves are also excited by abrupt rift opening and can be used to track and monitor the expansion of rifts (Olinger et al., 2022).

Most models of the wave response of ice shelves have focused exclusively on the flexural response. However, the Ross Ice Shelf data shows other wave modes, including the fundamental mode extensional Lamb wave that propagates close to the plane stress P-wave speed of ice and has dominantly horizontal displacements (Bromirski et al., 2017; Chen et al., 2018, 2019). These observations motivate us to examine how incident ocean waves convert to flexural gravity and extensional Lamb waves. Chen et al. (2018) suggest that wave-induced pressure changes on the shelf front, which exert a net horizontal force on the ice shelf, are responsible for excitation of extensional Lamb wave. We confirm this hypothesis with our modeling.

Before introducing our model, we remark on the many studies that have focused on the flexural gravity wave response of ice shelves and sea ice. Most work utilizes a bending plate model to describe the ice response, recognizing that horizontal wavelengths are much larger than ice thickness at frequencies of interest. The frequency-domain reflection/transmission problem of gravity waves in open water coupled to flexural gravity waves in ice-covered water was solved by Fox and Squire (1990, 1991). The earlier history of the field is reviewed by Squire et al. (1995); Squire (2007). While much of this work focused on sea ice, attention has shifted recently to ice shelves (Sergienko, 2010, 2013). Lipovsky (2018) provides a methodology to estimate wave-induced bending stresses from measured ice shelf motions. Finite element (Ilyas et al., 2018; Sergienko, 2017) and finite difference (Mattsson et al., 2018) methods can be used to solve to the potential flow problem in sub-shelf cavity. These studies show how the shallow water approximation breaks down at swell frequencies (Kalyanaraman et al., 2019) and how ice shelves affect the shoaling process as waves advance into shallower water (Meylan et al., 2021). Solution of the full elasticity problem in the ice shelf can be used to determine the validity of the plate approximation (Sergienko, 2010, 2017; Kalyanaraman et al., 2020). While most efforts focus on 2D vertical cross-section models, some 3D or 2D map-view models have been developed to account for the complex geometries and variable ice thickness and water depth of real ice shelves (Sergienko, 2017; Tazhimbetov et al., 2022). However, use of an bending plate model for the ice shelf precludes study of extensional Lamb waves and other ice shelf wave modes.

Our objective is to model the full-wave response of ice shelves, including ocean compressibility, ice elasticity and inertia, and gravity. We do this forna 2D vertical cross-section of the ice shelf and sub-shelf ocean cavity, coupled to an open-water region. The ice and ocean obey the elastic and acoustic wave equations, respectively, and gravity is added using an extension of the fully coupled method introduced by Lotto and Dunham (2015). This allows us to model extensional Lamb waves in addition to flexural gravity waves. A similar model was utilized by Kalyanaraman et al. (2020) to study wave reflection/transmission and resonance modes of finite length ice shelves. They note the existence of extensional wave resonance modes, but do not perform a systematic investigation of extensional Lamb wave excitation by incident surface gravity waves. This is the primary focus of our study and we anticipate results to be of use when interpreting data from ice shelves and understanding which wave modes might contribute to fracture and calving.

## 2 Model and wave modes

We study wave propagation in a 2D vertical cross-section of the ice shelf and sub-shelf ocean cavity, connected to an open-water region (Figure 1a). We use a coordinate system in which $x$ is horizontal and $z$ is vertical, positive up with the sea surface at $z = 0$ and seafloor at $z = -H_1$. An incident wave is imposed in the open-water region ($x < 0$) and arrives at the ice shelf edge ($x = 0$), where it is both reflected and transmitted into the ice shelf and sub-shelf cavity. In the open water ($x < 0$) the water depth is $H_1$. For $x > 0$, an ice shelf of thickness $H_i$ floats on the water. Given the ice and water densities, $\rho_i$ and $\rho_w$, respectively, hydrostatic balance requires the water depth in the sub-shelf cavity

to be $H_2 = H_1 - (\rho_i/\rho_w)H_i$. The top of the ice shelf is located at $z = (1 - \rho_i/\rho_w)H_i$. The ice-water interface is located $z = -(\rho_i/\rho_w)H_i$ and the sub-shelf ocean cavity extends to $z = -H_1$. When deriving dispersion relations involving the ice, it is convenient to introduce the half-thickness $h = H_i/2$.

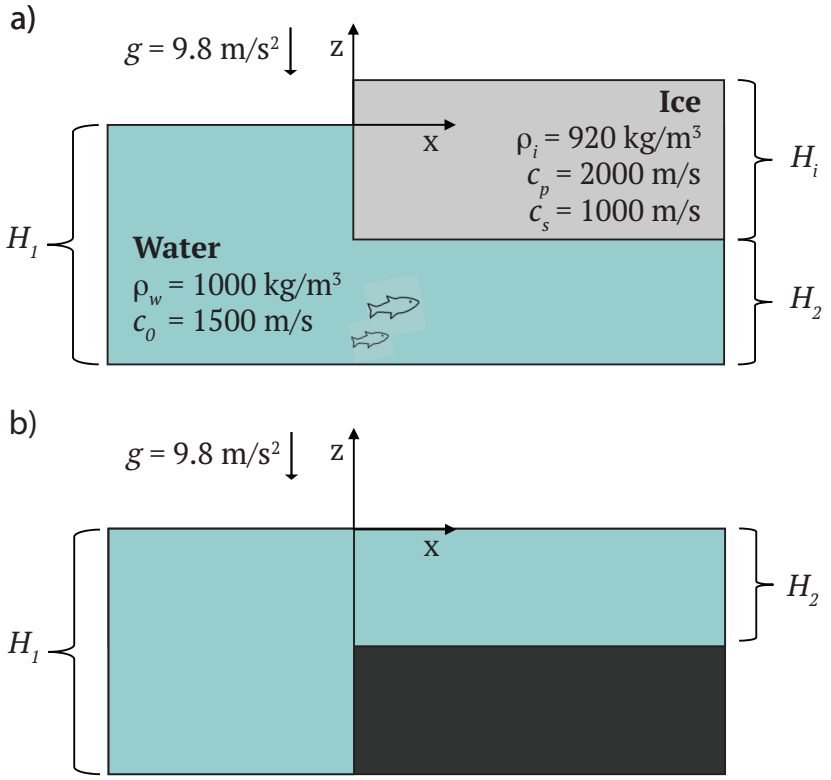


**Figure 1** a) An incident surface gravity wave, propagating to the right, reaches the ice shelf edge at $x = 0$, creating reflected surface gravity waves and transmitted flexural gravity and extensional Lamb waves. The ice shelf is of thickness $H_i$ and the ocean is of depth $H_1$ in open water and $H_2$ beneath the shelf. b) Step change in water depth at $x = 0$ that causes reflection and transmission of surface gravity waves, used to verify our procedure for calculating frequency-dependent reflection/transmission coefficients from time-domain simulations.

The ice and compressible ocean obey the elastic and acoustic wave equations, respectively, and gravity is added using an extension of the method introduced by Lotto and Dunham (2015), which assumes small perturbations about an initial hydrostatic equilibrium state in the water.

The governing equations in the water are

$$\frac{1}{K_w}\frac{\partial p}{\partial t} + \frac{\partial v_x}{\partial x} + \frac{\partial v_z}{\partial z} = 0, \tag{1}$$

obtained by combining the linearized mass balance with a linearized equation of state; and the momentum balance equations,

$$\rho_w \frac{\partial v_x}{\partial t} + \frac{\partial p}{\partial x} = 0, \tag{2}$$

and

$$\rho_w \frac{\partial v_z}{\partial t} + \frac{\partial p}{\partial z} = 0, \tag{3}$$

for particle velocities $v_i$, pressure perturbation $p$, bulk modulus $K_w$, and density $\rho_w$. The sound speed is $c_0 = \sqrt{K_w/\rho_w}$. Gravity acts as a restoring force, entering the open-water problem only through linearization of the free surface boundary condition,

$$\begin{aligned} p - \rho_w g\eta = 0, \quad & \text{at } x \\ < 0, & \ z \\ = 0, & \end{aligned} \tag{4}$$

where wave height $\eta$ is governed by the linearized kinematic condition on the sea surface,

$$\begin{aligned} \frac{\partial \eta}{\partial t} = v_z, \quad & \text{at } x \\ < 0, & \ z \\ = 0. & \end{aligned} \tag{5}$$

At the bottom of the ocean, we assume a rigid wall condition,

$$\begin{aligned} v_z &= 0, \quad \text{at } z \\ &= -H_1. \end{aligned} \tag{6}$$

The ice obeys the elastic wave equation for an isotropic solid with spatially uniform material properties:

$$\rho_i \frac{\partial^2 u_x}{\partial t^2} = (\lambda + \mu)\left(\frac{\partial^2 u_x}{\partial x^2} + \frac{\partial^2 u_z}{\partial x \partial z}\right) + \mu\left(\frac{\partial^2 u_x}{\partial x^2} + \frac{\partial^2 u_x}{\partial z^2}\right), \tag{7}$$

$$\rho_i \frac{\partial^2 u_z}{\partial t^2} = (\lambda + \mu)\left(\frac{\partial^2 u_x}{\partial x \partial z} + \frac{\partial^2 u_z}{\partial z^2}\right) + \mu\left(\frac{\partial^2 u_z}{\partial x^2} + \frac{\partial^2 u_z}{\partial z^2}\right), \tag{8}$$

for particle displacements $u_i$, density $\rho$, Lamé parameters $\lambda$ and $\mu$. The associated P- and S-wave speeds are $c_p = \sqrt{(\lambda + 2\mu)/\rho}$ and $c_s = \sqrt{\mu/\rho}$, respectively. To calculate stresses, we use Hooke's Law,

$$\sigma_{ij} = \lambda \epsilon_{kk} \delta_{ij} + 2\mu \epsilon_{ij}, \tag{9}$$

where $\delta_{ij}$ is the Kronecker delta, and the strain-displacement relation,

$$\begin{aligned} &\epsilon_{ij} \\ &\quad = \frac{1}{2}\left(\frac{\partial u_i}{\partial x_j} + \frac{\partial u_j}{\partial x_i}\right). \end{aligned} \tag{10}$$

The top of the ice is a free surface,

$$\begin{aligned} \sigma_{xz} &= 0, \quad \sigma_{zz} \\ &= 0, \quad \text{at } z \\ &= (1 - \rho_i/\rho_w) H_i. \end{aligned} \tag{11}$$

At the ice-water interface along the base of the ice shelf, we balance tractions and enforce continuity of normal velocity:

$$\sigma_{xz} = 0, \tag{12}$$

$$-\sigma_{zz} = p - \rho_w g \eta, \quad \partial \eta / \partial t = v_z, \tag{13}$$

$$\partial u_z / \partial t = v_z, \quad \text{at } x > 0,\ z = -(\rho_i/\rho_w) H_i, \tag{14}$$

where fields on the left side are evaluated at the bottom of the ice and fields on the right side are evaluated at the top of the water. Here the treatment of gravity in the water is identical to that in the open water region, with $\eta$ again being the vertical displacement at the top of the water. We are therefore accounting for pressure changes in response to perturbations about the background hydrostatic state in the water, but neglecting prestress within the ice.

Along the submerged portion of the vertical ice shelf edge, we again balance tractions and enforce continuity of normal velocity:

$$\sigma_{xz} = 0, \tag{15}$$

$$-\sigma_{xx} = p, \tag{16}$$

$$\partial u_x / \partial t = v_x, \quad \text{at } x = 0, \quad -(\rho_i/\rho_w) H_i < z < 0. \tag{17}$$

The portion of the shelf edge above water is a free surface:

$$\sigma_{xz} = 0, \tag{18}$$

$$\sigma_{xx} = 0, \quad \text{at } x = 0, \quad 0 < z < (1 - \rho_i/\rho_w) H_i. \tag{19}$$

Our goal is to study the reflection and transmission of incident surface gravity waves. Reflection and transmission coefficients of various wave modes can be defined in terms of the amplitude of propagating plane wave solutions in the frequency domain, which are derived in the following sections. However, we will extract these reflection and transmission coefficients from time-domain simulations using a procedure described subsequently.

## 2.1 Wave modes in open water

We first consider the problem of wave propagation in open water. We solve equations (1-3) with boundary conditions (4)-(6), assuming $e^{i(kx-\omega t)}$ dependence of all fields, where $k$ is the horizontal wavenumber and $\omega$ is the angular

frequency. For notational simplicity, $e^{i(kx-\omega t)}$ is implied and we denote the water depth as $H$. The solution for unit amplitude wave height ($\eta = 1$) is

$$p = \frac{\omega^2 \rho_w}{\kappa \sinh(\kappa H)} \cosh(\kappa(z+H)), \tag{20}$$

$$v_x = k\omega \frac{\cosh(\kappa(z+H))}{\kappa \sinh(\kappa H)}, \tag{21}$$

$$v_z = -i\omega \frac{\sinh(\kappa(z+H))}{\sinh(H\kappa)}, \tag{22}$$

where

$$\kappa = \sqrt{k^2 - \frac{\omega^2}{c_0^2}}, \tag{23}$$

and $\omega$ and $k$ are related by the dispersion relation

$$\omega^2 = g\kappa \tanh(H\kappa). \tag{24}$$

The solutions to (24) include surface gravity waves (with slight corrections due to water compressibility) and acoustic waves (with slight corrections due to gravity) and have be discussed in many previous studies (Sells, 1965; Yamamoto, 1982; Lotto and Dunham, 2015). In this study, we are exclusively interested in the surface gravity wave mode.

## 2.2 Wave modes in ice-covered water

In A, we solve the corresponding problem in ice-covered water. For notational simplicity, we denote the water depth as $H$ and the ice thickness as $2h$. The dispersion relation is

$$\frac{\omega \rho_w D_0}{\kappa \sinh(\kappa H)} = \frac{2\rho_i c_s^4}{\omega^3 p F}, \tag{25}$$

where

$$D_0 = \cosh(\kappa H) - \frac{g\kappa}{\omega^2} \sinh(\kappa H), \tag{26}$$

$$F = \frac{\sinh(ph)\sinh(qh)}{D_S} + \frac{\cosh(ph)\cosh(qh)}{D_A}, \tag{27}$$

$$D_S = 4k^2 pq \sinh(ph)\cosh(qh) - \left(k^2+q^2\right)^2 \cosh(ph)\sinh(qh), \tag{28}$$

$$D_A = 4k^2 pq \cosh(ph)\sinh(qh) - \left(k^2+q^2\right)^2 \sinh(ph)\cosh(qh), \tag{29}$$

with

$$p = \sqrt{k^2 - \omega^2/c_p^2}, \tag{30}$$

$$q = \sqrt{k^2 - \omega^2/c_s^2}. \tag{31}$$

Note that $D_0 = 0$ provides the dispersion relation for surface gravity waves in open water, given previously as (24). Similarly, $D_S = 0$ and $D_A = 0$ provide the dispersion relations for symmetric and antisymmetric modes of an elastic layer bounded by free surfaces.

Next we examine limits appropriate for long-wavelength extensional Lamb wave and flexural gravity wave modes. For the fundamental symmetric mode (extensional Lamb wave), assume $kh \ll 1$, such that $ph \ll 1$ and $qh \ll 1$. In this limit,

$$D_S \approx -\frac{\omega^2 qh}{c_s^4}\left(\omega^2 - k^2 c_{ps}^2\right), \tag{32}$$

where the plane stress P-wave speed $c_{ps}$ is defined via

$$c_{ps}^2 = 4c_s^2\left(1 - \frac{c_s^2}{c_p^2}\right). \tag{33}$$

Thus for an elastic plate bounded by free surfaces, solutions of $D_S = 0$, in this long-wavelength limit, describe nondispersive extensional Lamb waves propagating at $c_{ps}$.

For the fundamental antisymmetric mode (flexural wave), in addition to $kh \ll 1$, $ph \ll 1$, and $qh \ll 1$, we also assume $\omega/kc_p \ll 1$ and $\omega/kc_s \ll 1$ (phase velocity less than both the P- and S-wave speeds). In this limit, the dispersion relation for flexural waves in an elastic plate bounded by free surfaces, $D_A = 0$, can be written as

$$\omega^2 \approx \frac{4}{3}c_s^2\left(1-\frac{c_s^2}{c_p^2}\right)h^2k^4, \tag{34}$$

or equivalently

$$\omega^2 = \frac{B}{m}k^4, \tag{35}$$

where

$$B = \frac{2Eh^3}{3(1-\nu^2)}, \quad m = 2h\rho_i, \tag{36}$$

are the bending stiffness $B$ (written in terms of Young's modulus $E$ and Poisson ratio $\nu$) and the ice mass per horizontal unit area $m$. Note that

$$\frac{B}{m} = \frac{4}{3}c_s^2\left(1-\frac{c_s^2}{c_p^2}\right)h^2. \tag{37}$$

The approximate dispersion relation (35) matches that of flexural waves obeying the Euler-Bernoulli plate model,

$$-m\omega^2 w + B\frac{d^4w}{dx^4} = 0, \tag{38}$$

where $w$ is the vertical displacement (assumed to be uniform with depth).

Continuing with these approximations (which restricts focus to the flexural wave), but now accounting for the interaction of the ice shelf and water to study flexural gravity waves, we find

$$F \approx -\frac{c_s^4}{kh\omega^2\left(\omega^2 - \frac{B}{m}k^4\right)}, \tag{39}$$

such that the dispersion relation becomes

$$\frac{i\omega\rho_w\left[\cosh(kH) - \frac{gk}{\omega^2}\sinh(kH)\right]}{k\sinh(kH)} = \frac{m\omega^2 - Bk^4}{i\omega}, \tag{40}$$

or equivalently,

$$\frac{\rho_w\omega^2}{k\tanh(kH)} = Bk^4 + \rho_w g - m\omega^2. \tag{41}$$

This can be solved for $\omega$ as

$$\omega^2 = \frac{\rho_w g + Bk^4}{\rho_w/k\tanh(kH) + m}, \tag{42}$$

matching expressions given in many previous studies on flexural gravity waves (Ewing and Crary, 1934; Fox and Squire, 1990; Squire et al., 1995; Squire, 2007), thereby confirming the consistency of our model with known solutions in this limit.

Figure 2 shows the phase velocity ($c = \omega/k$) and group velocity ($U = d\omega/dk$) for the surface gravity wave, extensional Lamb wave, and flexural gravity wave modes. Parameter values are given in Table 1 and we use the open-water depth $H = H_1$ for the surface gravity wave and the sub-shelf depth $H = H_2$ for the extensional Lamb wave and flexural gravity wave solutions. We focus on frequencies up to 0.02 Hz, corresponding to the very long period ($< 0.003$ Hz) and infragravity ($0.003 - 0.02$ Hz) bands. We do not consider higher frequency swell in this study.

Surface gravity waves are normally dispersed, with phase and group velocity reaching a maximum wave speed of $\sqrt{gH}$ in the long wavelength limit (figure 2a). Extensional Lamb waves exhibit no significant dispersion over the frequency band of interest (figure 2b). In addition to gravity the elastic restoring force causes the flexural gravity waves to propagate faster than surface gravity waves, and shorter wavelengths propagate faster than longer wavelengths. Therefore, flexural gravity waves are anomalously dispersed, with phase and group velocity reaching a minimum wave speed of $\sqrt{gH}$ in the long wavelength limit (figure 2c). Additionally plotted in figure 2c are the group and phase velocity for the flexural gravity wave using the plate approximation (42), verifying the validity of the plate model at the frequencies of interest.

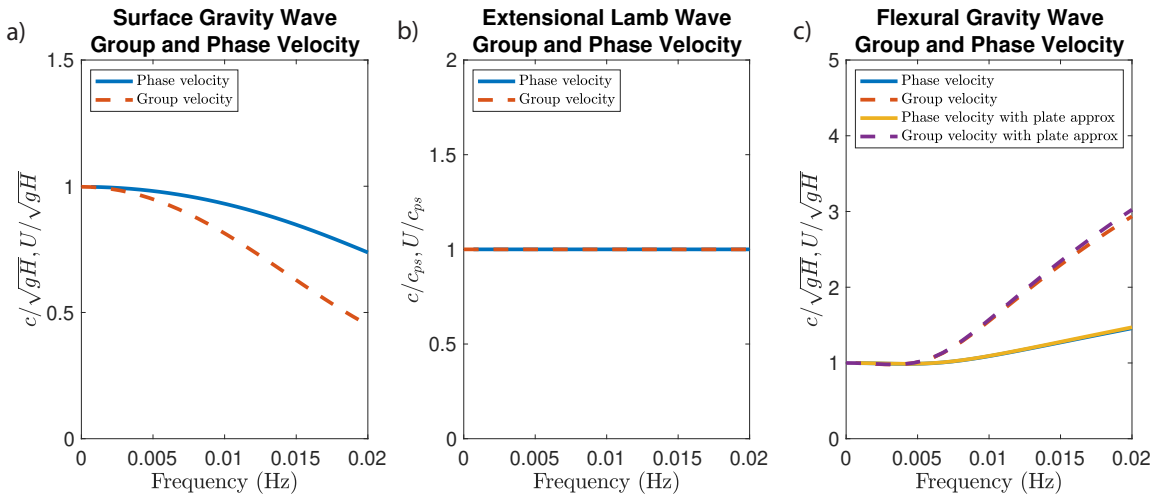


**Figure 2** Group and phase velocity for the surface gravity wave, extensional Lamb wave, and flexural gravity wave.

Finally, we remark that while our model results for the ice shelf response are discussed primarily in terms of wave amplitude (specifically, displacements of the ice surface), the horizontal normal stress $\sigma_{xx}$ is also of interest because this stress component acts to open and close vertical fractures and rifts. The stresses can be calculated immediately from the surface displacements using the frequency-domain transfer functions given by Lipovsky (2018). For flexural gravity waves, which carry the largest stresses, the stress $\sigma_{xx}$ can be obtained from the vertical displacement $w$, in the long wavelength plate theory limit, as (Timoshenko and Goodier, 1970)

$$\sigma_{xx} \approx -\frac{6Bk^2}{H_i^2} w. \tag{43}$$

# 3 Procedure to extract reflection and transmission coefficients from time-domain simulations

In this section we describe a procedure to extract frequency-dependent reflection and transmission coefficients from our time-domain simulations. The procedure will utilize Fourier transforms in both space and time with the following notation:

$$\tilde{f}(k,t) = \int_{-\infty}^{\infty} f(x,t) e^{-ikx}\, \mathrm{d}x\,, \tag{44}$$

$$f(x,t) = \frac{1}{(2\pi)} \int_{-\infty}^{\infty} \tilde{f}(k,t) e^{ikx}\, \mathrm{d}k \tag{45}$$

$$\hat{f}(x,\omega) = \int_{-\infty}^{\infty}\int_{-\infty}^{\infty} f(x,t) e^{i\omega t}\, \mathrm{d}t\,, \tag{46}$$

$$f(x,t) = \frac{1}{2\pi} \int_{-\infty}^{\infty} \hat{f}(x,\omega) e^{-i\omega t}\, \mathrm{d}\omega\,. \tag{47}$$

## 3.1 Surface gravity wave reflection/transmission for a step change in water depth

We begin with the simpler problem of surface gravity wave reflection/transmission from a step change in water depth. There is no ice shelf in this problem. Let $H_1$ and $H_2$ be the water depths in $x < 0$ and $x > 0$, respectively (Figure 1b). The problem is posed in the frequency domain. Define $k_1$ and $k_2$ as the wavenumbers of the surface gravity wave mode in $x < 0$ and $x > 0$, respectively, obtained by solving the open-water dispersion relation (24). The wavefield solution in the frequency domain, for an incident wave of spectral amplitude $A(\omega)$, is given by

$$\hat{\eta}(x,\omega) = \begin{cases} A(\omega)\left[e^{ik_1 x} + R(\omega)e^{-ik_1 x}\right] + \text{other modes}, & x < 0, \\ A(\omega)T(\omega)e^{ik_2 x} + \text{other modes}, & x > 0, \end{cases} \tag{48}$$

where $R$ and $T$ are the frequency-dependent reflection and transmission coefficients, respectively, for the propagating surface gravity wave mode. In addition, it is well known that except in the shallow water limit, there are additional evanescent surface gravity wave mode solutions to (24), which are confined to the vicinity of the step change in water depth at $x = 0$ (Newman, 1965; Miles, 1967; Dingemans, 1997). These modes can be safely ignored at locations $x$ sufficiently removed from $x = 0$. Furthermore, because we account for water compressibility, there are also acoustic

modes. The acoustic modes exist as propagating waves only above some cut-off frequency, which is much higher than the frequencies of interest to us. Thus these modes are also evanescent and can be neglected in the following procedure to determine $R$ and $T$.

Our goal now is to set up a problem in the time domain from which we can extract $R$ and $T$. To do this, we set initial conditions at $t = 0$ corresponding to a broadband incident wave packet propagating only in the $+x$ direction. Define $\eta(x, 0) = \eta_0(x)$ and its spatial Fourier transform

$$\tilde{\eta}_0(k) = \int \eta_0(x) e^{-ikx} dx. \tag{49}$$

The wavefield at some later time $t$ is obtained by multiplying by the phase factor $e^{-i\omega_1 t}$, where $\omega_1 = \omega_1(k)$ is obtained from solving the dispersion relation (24) for the surface gravity wave mode in water of depth $H_1$. We select the sign of $\omega_1$ such that $\omega_1/k > 0$ so that the wave propagates in the $+x$ direction.

Next we switch between $\omega$ and $k$ Fourier transforms using a change of variable based on the dispersion relation. Note that $d\omega = U dk$, where $U$ is the group velocity, which can be viewed as either a function of $k$ or $\omega$, as desired, provided that these are evaluated using the solution to the dispersion relation corresponding to the desired surface gravity wave mode. This procedure is illustrated for the incident wave:

$$\eta^I(x,t) = \frac{1}{2\pi} \int \tilde{\eta}_0(k) e^{i(kx - \omega_1 t)} dk \tag{50}$$

$$= \frac{1}{2\pi} \int \frac{\tilde{\eta}_0(k_1)}{U(k_1)} e^{i(k_1 x - \omega t)} d\omega, \tag{51}$$

where $k_1 = k_1(\omega)$ is evaluated for the surface gravity wave mode in water of depth $H_1$. It follows that

$$\hat{\eta}^I(x,\omega) = \int \eta^I(x,t) e^{i\omega t} dt \tag{52}$$

$$= \frac{\tilde{\eta}_0(k_1)}{U(k_1)} e^{ik_1 x}, \tag{53}$$

from which we identify the spectral amplitude of the incident wave in (48) as

$$A(\omega) = \tilde{\eta}_0(k_1)/U(k_1). \tag{54}$$

Initial conditions on pressure and particle velocity are obtained by evaluating (20)-(22) times the surface displacement spectral amplitude $A(\omega)$.

To solve for the reflection coefficient $R$ from our time-domain simulation, we Fourier transform the time series of $\eta$ at some point $x < 0$ to obtain $\hat{\eta}(x, \omega)$. Then solve (48), neglecting the evanescent surface gravity and acoustic modes, to obtain

$$R(\omega) = \left[ \frac{\hat{\eta}(x,\omega)}{A(\omega)} - e^{ik_1 x} \right] e^{ik_1 x}. \tag{55}$$

The procedure can be simplified even further by selecting the $x$ location to be to the left of the initial wave packet, so that only the reflected wave contributes to the time series. In this case, the incident wave in (55), namely the $-e^{ik_1 x}$ term in brackets, can be ignored.

Extracting the transmission coefficient is similar. We select some point $x > 0$ sufficiently far from $x = 0$, extract the time series of $\eta$, and Fourier transform it in time to obtain $\hat{\eta}(x, \omega)$. Neglecting evanescent surface gravity and acoustic modes, we solve (48) for the transmission coefficient

$$T(\omega) = \frac{\hat{\eta}(x,\omega)}{A(\omega)} e^{-ik_2 x}. \tag{56}$$

While the procedure above is stated for a single $x$, in our implementation we average the resulting $R$ and $T$ over multiple $x$, which we find improves the accuracy at high frequencies. With a grid spacing of 200 m $R$ was averaged over $x = -100$ km to $-50$ km and $T$ was averaged over $x = -100$ km to $-50$ km.

The procedure above does require neglecting evanescent surface gravity and acoustic wave modes, which might introduce a small error in the calculated $R$ and $T$. This error could be eliminated using a more sophisticated procedure that isolates a specific wave mode. For example, it is well known that the eigenfunctions of wave modes in layered media obey orthogonality conditions (Aki and Richards, 2002). The orthogonality conditions require evaluation of integrals of particle velocity and stress fields over depth $z$ at fixed $x$. We defer this extension to future work.

### 3.2 Reflection/transmission with an ice shelf

The procedure for extracting reflection/transmission coefficients for the ice shelf problem (Figure 1a) is more complex, as we are interested in multiple wave modes, not all of which are well expressed in the water surface vertical displacement $\eta$. Furthermore, we note that seismometers placed on the ice shelf surface are the primary means of measuring wave motions. Thus we define $u(x,t)$ and $w(x,t)$ as the horizontal and vertical displacements of the top surface of the ice shelf.

The incident and reflected wavefield in the open-water region ($x < 0$) is identical to that in (48). The surface displacements of the transmitted wavefield can be written as

$$\hat{u}(x,\omega) = A(\omega)\left[T_{x,f}(\omega)e^{ik_f x} + T_{x,e}(\omega)e^{ik_e x}\right] + \text{other modes}, \tag{57}$$

$$\hat{w}(x,\omega) = A(\omega)\left[T_{z,f}(\omega)e^{ik_f x} + T_{z,e}(\omega)e^{ik_e x}\right] + \text{other modes}, \tag{58}$$

where the subscript $x$ or $z$ on the transmission coefficients $T$ refers to the displacement direction and the subscripts $f$ and $e$ refers to the flexural gravity and extensional Lamb wave modes, respectively. The wavenumbers $k_f$ and $k_e$ are obtained from the flexural gravity and extensional Lamb wave solutions of the dispersion equation (107). We note that the ratios $T_{x,f}/T_{z,f}$ and $T_{x,e}/T_{z,e}$ are independent of the reflection/transmission process and can be determined from the eigenfunctions given in A. Thus we need only consider one displacement direction when extracting transmission coefficients for each wave mode. Because flexural gravity waves have dominantly vertical particle motions, we focus on $T_{f,z}$. Similarly, because extensional Lamb waves have dominantly horizontal particle motions, we focus on $T_{e,x}$.

The procedure for extracting the reflection coefficient of surface gravity waves is identical to the previous problem. To extract transmission coefficients, we record ice surface displacement time series $u$ and $w$ at some $x > 0$ that is sufficiently far from the ice shelf edge. We then exploit the vastly different phase and group velocities of the flexural gravity and extensional Lamb wave modes by windowing the appropriate wave arrivals in the time series. We then Fourier transform these windowed time series in time and evaluate

$$T_{z,f}(\omega) = \frac{\hat{w}(x,\omega)}{A(\omega)}e^{-ik_f x}, \tag{59}$$

$$T_{x,e}(\omega) = \frac{\hat{u}(x,\omega)}{A(\omega)}e^{-ik_e x}. \tag{60}$$

### 3.3 Numerical simulations

In this study we utilize the finite difference code FDMAP (Dunham et al., 2011; Kozdon et al., 2012, 2013) that couples an acoustic ocean in the presence of gravity to an elastodynamic solids. We employ a Cartesian mesh with uniform (but different) grid spacings in the $x$ and $z$ directions. The method uses sixth-order central differences in space in the interior (with reduced order near boundaries and interfaces) and a third-order explicit Runge-Kutta method for time-stepping. Gravity is accounted for using the method in Lotto and Dunham (2015), for both the open-water region and at the top of the sub-shelf water cavity.

We examine two model geometries. For the open ocean with a floating ice shelf and subshelf cavity problem setup (Figure 1a), the domain extends from $x = -100$ km to $x = 300$ km with the ice shelf edge located at $x = 0$. In the $x-$direction the grid spacing is 200 m. In the $z-$direction the domain is divided into 3 blocks. From the seafloor, $z = -H_1 = -1$ km, to the depth of the ice-water interface, $z = -(\rho_i/\rho_w)H_i = -0.368$ km, the grid spacing in the $z-$direction is 13.45 m (48 grid points). From the depth of the ice-water interface, $z = -(\rho_i/\rho_w)H_i = -0.368$ km, to the open-water free surface $z = 0$ the grid spacing in the $z-$direction is 5.84 m (64 grid points). From the open-water free surface $z = 0$ to the top of the ice shelf, $z = (1-\rho_i/\rho_w)H_i = 0.032$ km, the grid spacing in the $z-$direction is 2.29 m (14 grid points). Characteristic-based absorbing boundary conditions (Kozdon et al., 2012, 2013) are used on the left and right sides of the domain. The simulation runs for a total of 1700 s with time steps of 0.000615 s.

For the step change in water depth problem setup, figure 1b, the domain extends from $x = -400$ km to $x = 400$ km with the step changing occurring at $x = 0$. In the $x-$direction the grid spacing is 200 m. In this setup $H_1 = 1$ km and $H_2 = 0.25$ km with 10 m grid spacing in the $z-$direction. The simulation runs for a total of 8000 s with time step of 0.003333 s.

## 4 Reflection and transmission coefficients for a step change in water depth

Before proceeding to the ice shelf reflection/transmission problem, we verify our model and procedure for extracting $R$ and $T$ on a problem with a known solution. Specifically, we consider a step change in water depth, from $H_1$ to $H_2$ at $x = 0$ (Figure 1b).

The reflection/transmission coefficients in the linear long wave (LLW, $k_1 H_1 \ll 1$ and $k_2 H_2 \ll 1$) limit are well known (Lamb, 1905):

$$R_{LLW} = \frac{\sqrt{H_1} - \sqrt{H_2}}{\sqrt{H_1} + \sqrt{H_2}}, \tag{61}$$

**Table 1** Parameter values for dispersion analysis and simulations.

| parameter | symbol | value |
|---|---|---|
| Density in ocean | $\rho_w$ | 1000 kg/m$^3$ |
| Sound speed in ocean | $c_0$ | 1500 m/s |
| Density in ice | $\rho_i$ | 920 kg/m$^3$ |
| P-wave speed in ice | $c_p$ | 2000 m/s |
| S-wave speed in ice | $c_s$ | 1000 m/s |
| Gravity | $g$ | 9.8 m/s$^2$ |
| Open water ocean depth | $H_1$ | 1000 m |
| Sub-shelf ocean cavity | $H_2$ | 632 m |
| Ice thickness | $H_i$ | 400 m |

and the transmission coefficient is

$$T_{LLW} = \frac{2\sqrt{H_1}}{\sqrt{H_1} + \sqrt{H_2}}. \tag{62}$$

These values are the anticipated limits for $R$ and $T$ in the low frequency limit.

Exact closed form expressions for $R$ and $T$ are not available outside the LLW limit, and instead the problem must be solved numerically or using approximations (Newman, 1965; Miles, 1967; Dingemans, 1997). However, in the high frequency limit, surface gravity waves will be confined to the water surface and will not sense the change in water depth. Hence the high frequency limits are $R \to 0$, $T \to 1$.

### 4.1 Simulation results

Our initial vertical sea surface displacement is a unit amplitude Gaussian,

$$\eta_0(x) = \exp\left\{\left(\frac{-(x-x_0)^2}{2\sigma^2}\right)\right\}, \tag{63}$$

where $x_0$ is the center of the Gaussian and $\sigma$ is the width of the Gaussian. We set $x_0 = -15$ km and $\sigma = 1$ km, which provides a wave packet that includes dispersive surface gravity waves at frequencies above the LLW limit. We use the eigenmode solution and Fourier transforms in the $x$ direction (using FFTs on the simulation grid) to determine the pressure and particle velocities in the water corresponding to a wave packet propagating in the $+x$ direction with surface amplitude (63). The initial conditions are shown in figure 3 and time-domain simulation results are shown in figure 4. Normal dispersion is visible at high frequencies. Because $H_2 < H_1$, the reflection coefficient is positive and the transmission coefficient is greater than unity.

### 4.2 Reflection and transmission coefficients

From the simulation data, we extract the simulation reflection and transmission coefficients using (55) and (56), respectively. Results are shown in figure 5. The reflection and transmission coefficients match the LLW solutions, given in (61) and (62), in the low frequency limit, but differ at high frequency as seen in previous studies (Newman, 1965; Miles, 1967; Dingemans, 1997).

## 5 Reflection and transmission coefficients for ice-covered water

Having verified our procedure for determining reflection and transmission coefficients from time-domain simulations, we now turn to the problem of wave interaction with floating ice shelves (Figure 1a).

### 5.1 Simulation results

We use the same initial conditions for the wave packet as used in the step change in depth problem. Incident surface gravity waves in the open water impact the ice shelf, exciting both flexural gravity and extensional Lamb waves. The flexural gravity waves are dominantly expressed in the vertical components (figure 6) and extensional Lamb waves are dominantly expressed in the horizontal component (figure 7). We also show the horizontal normal stress $\sigma_{xx}$ in figure 8. The largest stresses are carried by flexural gravity waves, not extensional Lamb waves.

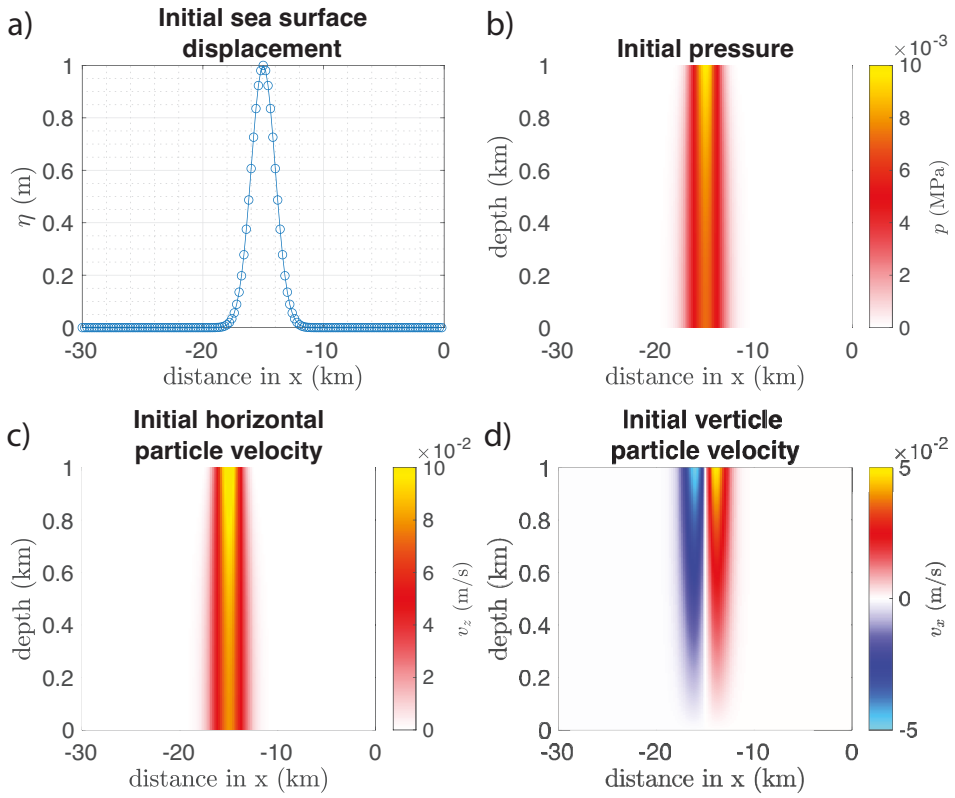


**Figure 3** Simulation initial conditions: a) sea surface displacement, b) pressure, c) horizontal particle velocity, d) vertical particle velocity.

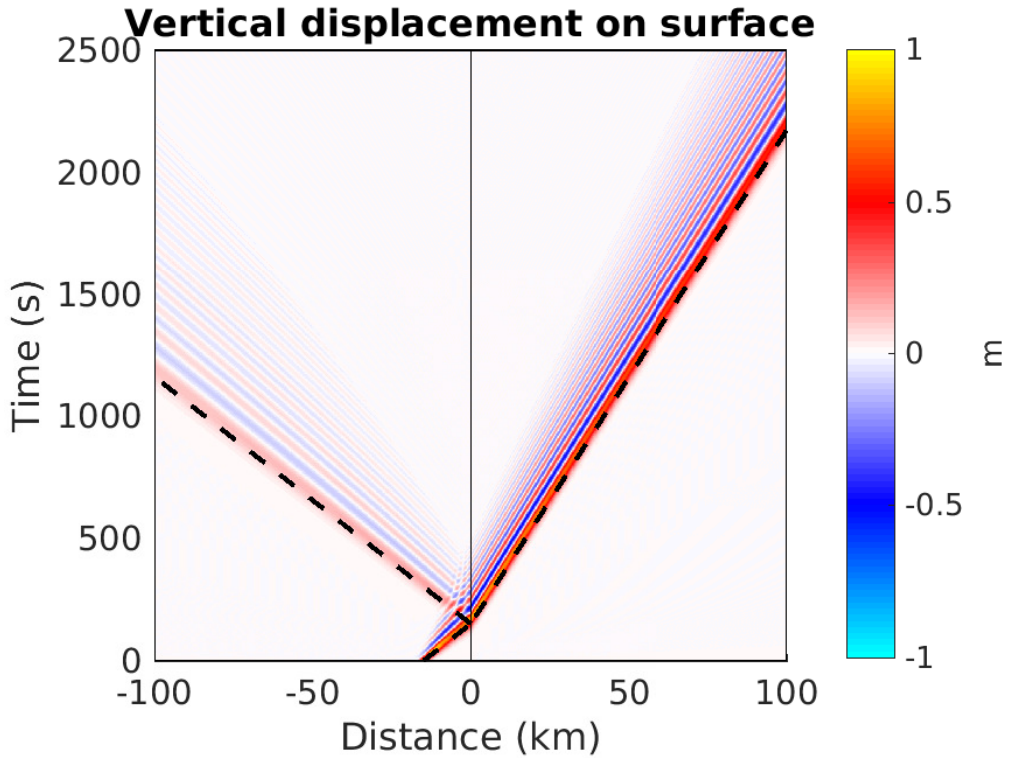


**Figure 4** Simulation results for the step change in water depth problem, showing vertical displacement on the surface ($z = 0$) through time.

## 5.2 Reflection and transmission coefficients

Following the procedure described in section 3.2, we calculate reflection and transmission coefficients. Results are shown in Figure 9. We begin by explaining the reflection and transmission of surface gravity and flexural gravity

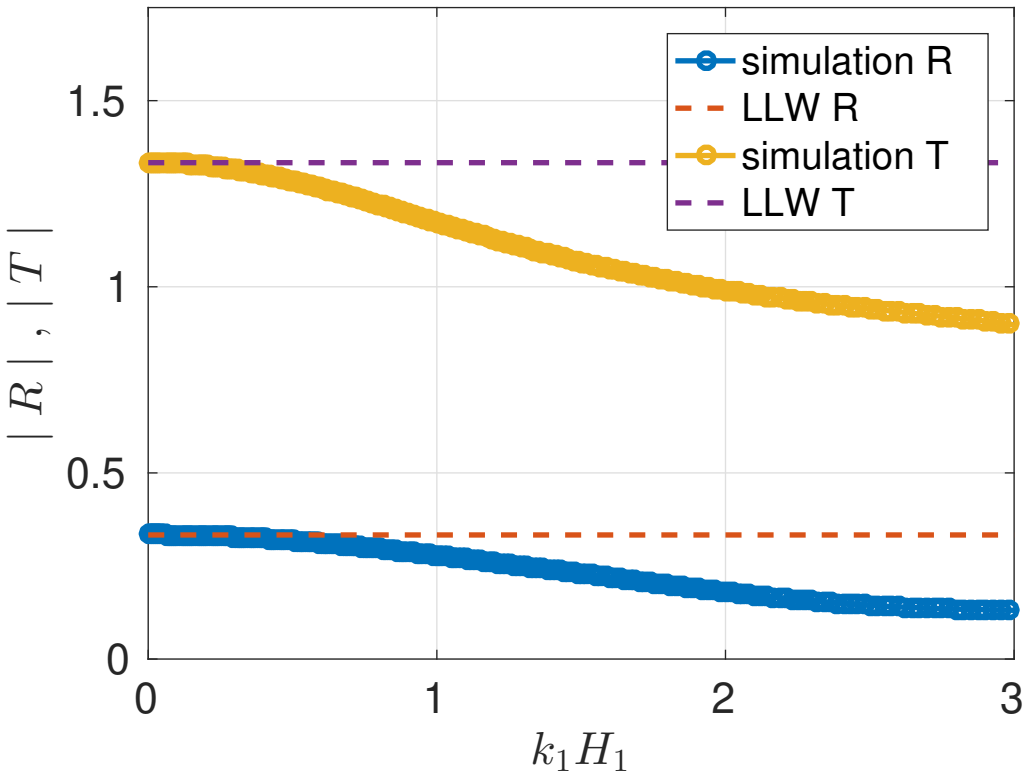


**Figure 5** Reflection and transmission coefficients for the step change in water depth problem, which approach the linear long wave (LLW) solution in the low frequency limit.

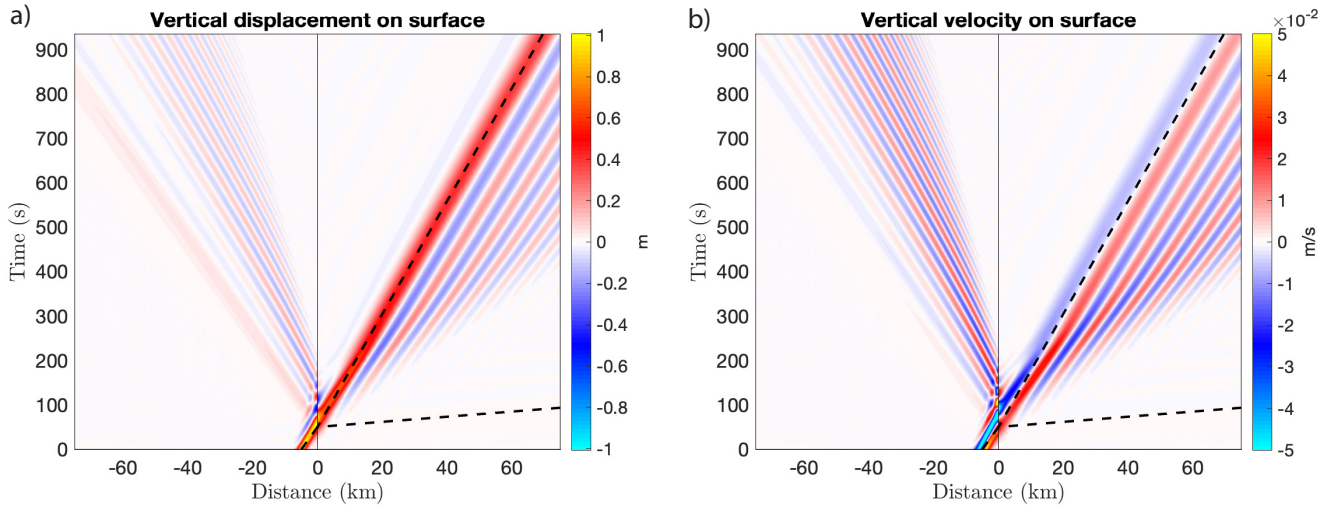


**Figure 6** (a) Vertical displacement and (b) vertical velocity on the open-water and ice surface. Surface gravity waves in the open-water region are normally dispersed with the longest wavelengths traveling at the linear long wave speed $\sqrt{gH_1}$. The ice shelf response is dominated by anomalously dispersed flexural gravity waves, with the longest wavelengths traveling at the linear long wave speed $\sqrt{gH_2}$.

waves (Figure 9a), both quantified in terms of the vertical displacement amplitude on the water or ice surface. At low frequencies, the results match expectations from linear long wave theory without ice, illustrating that the additional inertia and elastic resistance to flexure of the ice are negligible. Because $H_2 < H_1$, $T > 1$ in this limit. As frequency increases, $R$ and $T$ both decrease, as seen for the step change in depth problem without ice (Figure 5). The decrease of $R$ for this problem arises from the shorter wavelength waves, which involve motions of the water at depths of order the wavelength, becoming less sensitive to the water depth. In the high frequency limit, the waves simply propagate across the step without reflection. In contrast, for the ice shelf problem, the reflection coefficient begins increasing around 0.01 Hz as the stiffness and inertia of the ice shelf begin to impede wave transmission. The anticipated high frequency limit for $R$ is unity, meaning that surface gravity waves are fully reflected.

Next we examine transmission of extensional Lamb waves, which we quantify in terms of the horizontal displacement amplitude on the ice surface (Figure 9c,d). The transmission coefficient increases as frequency decreases,

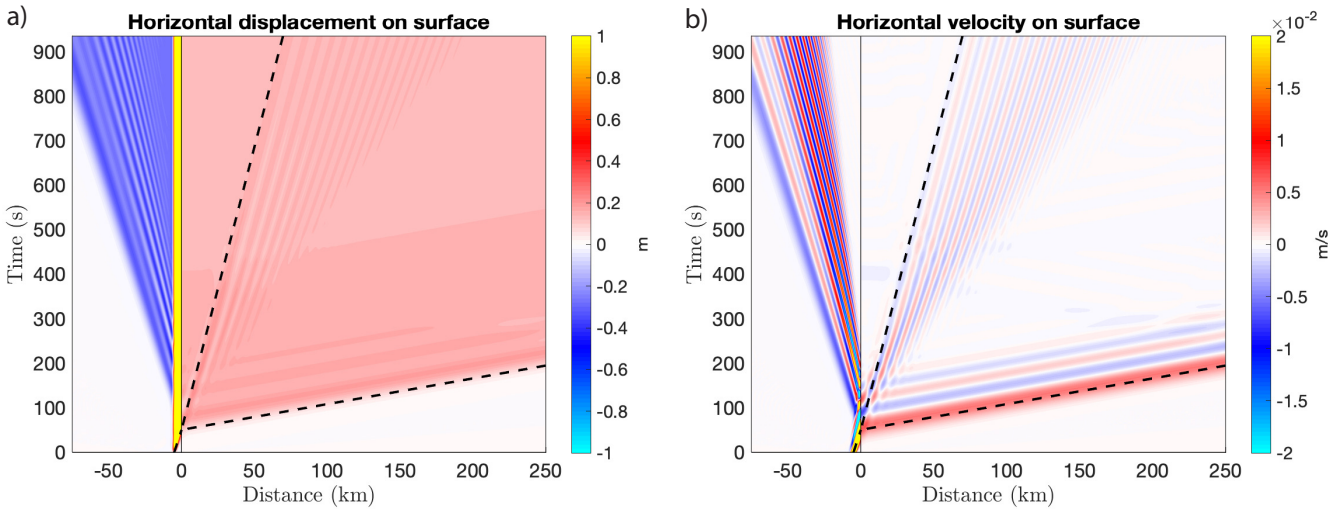


**Figure 7** (a) Horizontal displacement and (b) horizontal velocity on the open-water and ice surface. In addition to surface gravity waves in the open-water region and flexural gravity waves in the ice-covered water are both visible, we also see extensional Lamb waves. These have minimal dispersion, dominantly horizontal particle motions, and propagate around the plane stress P-wave speed of ice.

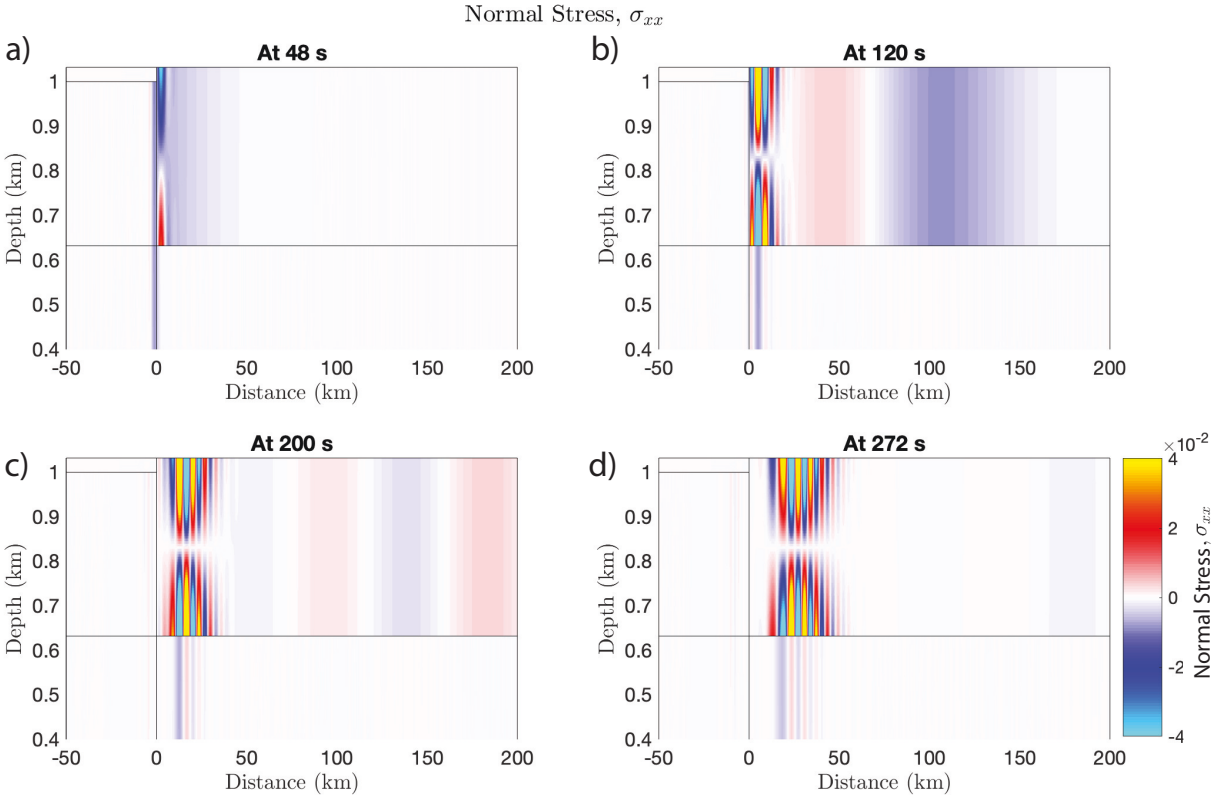


**Figure 8** Tensile and compressional horizontal normal stresses ($\sigma_{xx}$) in the ice and minus pressure ($-p$) in the water, highlight the propagating long wavelength extensional Lamb waves and shorter wavelength flexural gravity waves. The extensional Lamb wave exhibits symmetric stressing about the centerline of the ice shelf, whereas the flexural gravity wave exhibits antisymetric stressing. The largest stress changes are carried by the flexural gravity waves.

passing through unity around 0.001 Hz. Transmission coefficients larger than unity indicate that horizontal displacements of the ice surface carried by extensional Lamb waves exceed vertical displacements of the incident waves. In the low frequency limit, $T$ diverges as $\omega^{-1}$, a behavior that we explain in the next section.

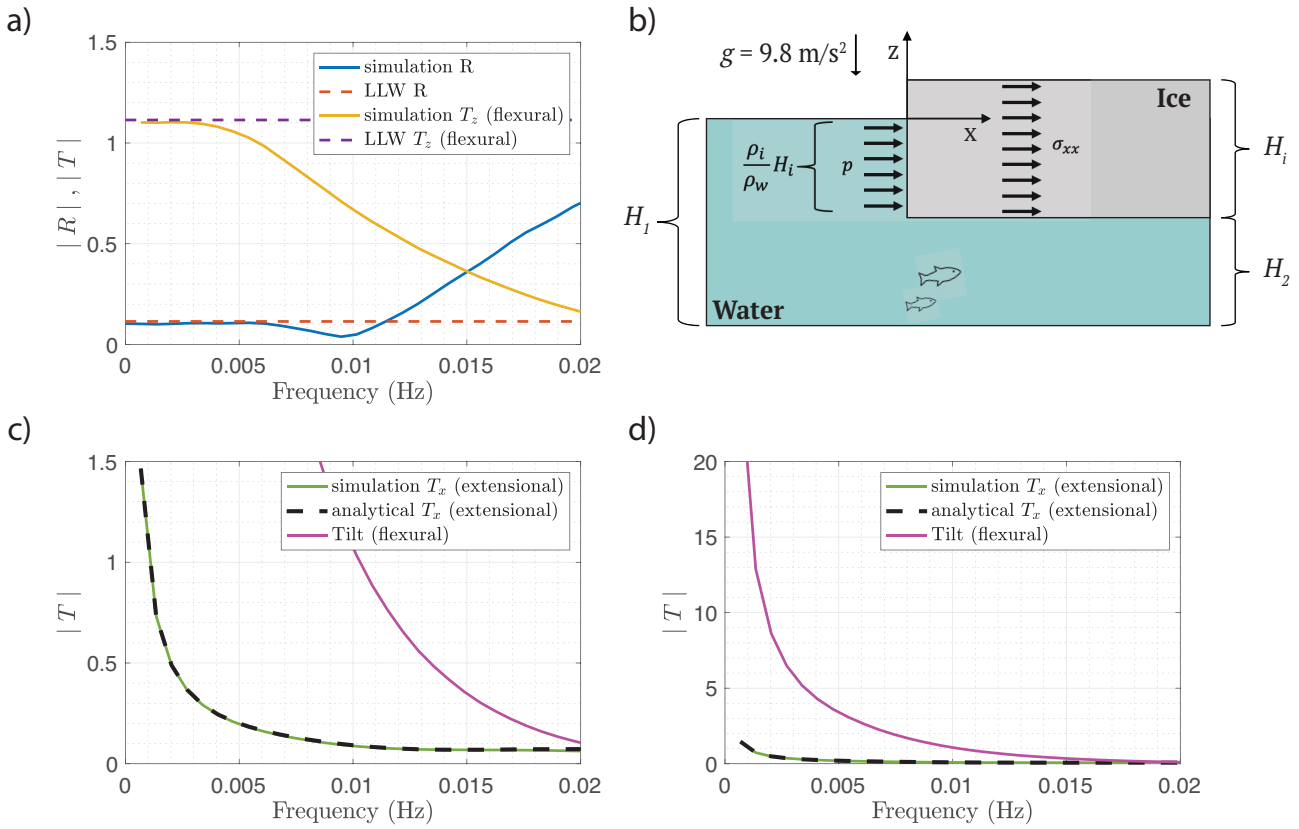


**Figure 9** (a) Simulation-derived reflection coefficient (blue) and flexural gravity wave vertical transmission coefficient (yellow) with linear long wave limits for the step depth change problem (red and purple). (b) Diagram illustrating extensional Lamb wave excitation by pressure changes exerted on the ice shelf face by surface gravity waves. (c and d) Simulation-derived extensional Lamb wave horizontal transmission coefficient (green), the analytical prediction for the transmitted extensional wave given in equation (66) (black dashed), and and flexural gravity wave tilt contribution to horizontal seismometer measurements given by equation (68) (magenta).

## 5.3 Mechanism for extensional Lamb wave excitation

In this section we provide a quantitative theory for the excitation of extensional Lamb waves by incident surface gravity waves. The incident waves cause pressure changes in the water column and these pressure changes exert a horizontal force on the submerged portion of the ice shelf edge. This excites extensional Lamb waves. This conceptual mechanism was suggested by Chen et al. (2018), which we extend quantitatively as follows.

Consider an incident, time-harmonic surface gravity wave of amplitude $A$. The wave amplitude at the ice shelf edge differs from $A$ because of the superposition of incident and reflected waves. By neglecting evanescent modes, we approximate the amplitude at the edge as $(1 + R)A$, where $R$ is the frequency-dependent surface gravity wave reflection coefficient. Next we estimate the pressure change in the water column associated with the surface gravity waves as $p = \rho_w g(1 + R)IA$, where

$$I(\omega) = \frac{\rho_w}{\rho_i H_i} \int_{-(\rho_i/\rho_w)H_i}^{0} \frac{\cosh(k(z + H_1))}{\cosh(kH_1)} dz, \tag{64}$$

is the normalized integral of the depth-dependent pressure changes from the eigenmode solution given in A and $k$ is the wavenumber of surface gravity waves at angular frequency $\omega$. The normalization is chosen so that $I \to 1$ in the low frequency limit ($kH_i \ll 1$) where pressure changes are approximately uniform over the submerged portion of the shelf front. We find that $I \approx 1$ over frequencies of interest in this study. This pressure change gives rise to a net horizontal force

$$\begin{aligned} F &= p\frac{\rho_i}{\rho_w} H_i \\ &= \rho_i g(1 + R)IAH_i. \end{aligned} \tag{65}$$

Next we assume that this force generates an effectively 1D extensional Lamb wave with depth-independent normal stress $\sigma_{xx}$ and horizontal particle velocity $v_x$. The depth-independence of these fields holds asymptotically in the limit of horizontal wavelengths greatly exceeding ice thickness, as evident from the eigenfunctions in A. This limit

is well justified for frequencies of interest. The stress and particle velocity are related by the extensional Lamb wave impedance: $-\sigma_{xx} = \rho_i c_{ps} v_x$, where we have assumed that the phase velocity is approximately $c_{ps}$ (Figure 2b). Force balance requires $F = -\sigma_{xx} H_i$, such that $-\sigma_{xx} = \rho_i g(1+R)IA$. Inserting this into the impedance relation, we obtain $v_x = (g/c_{ps})(1+R)IA$. Finally, using $v_x = -i\omega u_x$, we obtain the extensional Lamb wave transmission coefficient (defined as the ratio $u_x/A$)

$$T_{x,e}(\omega) = \frac{ig[1+R(\omega)]I(\omega)}{\omega c_{ps}}. \tag{66}$$

This prediction, using the $R(\omega)$ derived from the simulations, is plotted in Figure 9c,d. There is excellent agreement with the simulation-derived $T_{x,e}(\omega)$. We note that in the low frequency limit (i.e., very long period band), where the ice has negligible effect on gravity wave propagation, except by modifying the water depth, we can approximate $R(\omega) \approx R_{LLW}$, which is independent of frequency, and $I(\omega) \approx 1$. This reveals the $T_{x,e} \propto \omega^{-1}$ divergence seen in our simulation results (Figure 9c,d).

## 5.4 Tilt contribution to horizontal seismometer measurements

Our theory and simulation results provide a prediction of both horizontal and vertical displacements of the ice shelf surface, which can be compared to seismic observations. Here we combine previous results to predict the frequency-dependent ratio of horizontal to vertical displacements. We assume that horizontal displacements are dominated by extensional Lamb waves and that vertical displacements are dominated by flexural gravity waves. The predicted displacement ratio is therefore approximated as $|u_x|/|u_z| \approx |T_{x,e}(\omega)|/|T_{z,f}(\omega)|$. We focus on the low frequency limit where the ice has minimal influence on flexural gravity waves, except by reducing the water depth, so that $T_{z,f}(\omega)$ can be approximated as the LLW transmission coefficient (62). Similarly, the surface gravity wave reflection coefficient can be approximated using (61). Then, using these results in (66), and noting that for the LLW problem $1 + R_{LLW} = T_{LLW}$, we find the predicted horizontal-to-vertical displacement ratio

$$|u_x|/|u_z| \approx \frac{g}{\omega c_{ps}} \approx \frac{1\ \text{mHz}}{f}, \tag{67}$$

with the latter expression using the value of $c_{ps}$ for our simulation parameters. Thus vertical displacements are predicted to be larger than horizontal displacements for frequencies greater than ~1 mHz, whereas horizontals will be larger for lower frequencies.

This prediction is in apparent contradiction to observations, which can be found in power spectral density plots for horizontal and vertical seismometer data in Figure 3 of Bromirski et al. (2017). The observations show larger horizontal motions not just in the very long period band but also in the infragravity band. There are several possible explanations for this discrepancy. First, there could be some additional extensional Lamb wave source that is unaccounted for in our model. Turbulent drag along the base of the ice shelf during wave motions in the sub-shelf cavity would provide an additional horizontal force that would excite extensional Lamb waves. Drag of this form is widely used in shallow water wave modeling, with basal shear stress (drag) being proportional to the square of horizontal velocity. Given that this is a nonlinear forcing mechanism, frequency-dependent excitation of extensional waves cannot be quantified without detailed modeling of the broadband wavefield. We defer this to future work. Another hypothesis is that the horizontal seismometer components are not only measuring horizontal displacements, but also include contributions from tilt. Tilt effects are most important at low frequencies, and studies of atmospheric coupling to the solid Earth have identified tilt as important or even dominant at the frequencies of interest to us (Rodgers, 1968; Tanimoto and Wang, 2018).

To explore this possibility, we follow Rodgers (1968) by calculating the tilt contribution to horizontal seismometer measurements as

$$\begin{aligned} u_{h,\text{tilt}} &= -\frac{g}{\omega^2}\frac{\partial \hat{w}(x,\omega)}{\partial x} \\ &= -\frac{igk}{\omega^2}\hat{w}, \end{aligned} \tag{68}$$

where the subscript $h$ denotes the seismometer horizontal component and $\hat{w}$ is the vertical displacement of the surface in the frequency domain. The final expression follows by assuming $e^{ikx}$ dependence of the propagating wave, where $k$ is the wavenumber for a given wave mode at angular frequency $\omega$.

We calculate the tilt contribution from both extensional Lamb and flexural gravity waves, taking $\hat{w}$ from our simulations as before, which we normalize by the amplitude of the incident surface gravity wave. We find that the contribution from extensional Lamb waves is negligible in comparison to the actual horizontal displacements carried by these waves. In contrast, the tilt contribution from flexural gravity waves, which is shown in Figure 9c,d, is larger than the horizontal extensional Lamb wave displacements over the entire frequency band of our study. Specifically, flexural gravity wave tilt is an order of magnitude larger than extensional Lamb wave horizontals at frequencies ~0.001 Hz characterizing the very long period band. This ratio decreases toward unity in the infragravity wave band. Thus we conclude that horizontal component seismometers are primarily measuring tilt from flexural gravity waves, especially at low frequencies.

Additional features of the seismic observations support this idea. Figure 9 of Chen et al. (2018) provides cross-correlation-based seismograms, bandpassed to 0.002-0.004 Hz, showing move-out at the flexural gravity wave speed on both vertical and horizontal components. The beamforming dispersion analysis in their Figure 8 shows larger power on the horizontal component than the vertical component along the flexural gravity wave dispersion curve at frequencies less than 0.02 Hz. This is inconsistent with the expected horizontal to vertical ratio for flexural gravity waves, but at least qualitatively consistent with our results in Figure 9.

# 6 Conclusion

In this work we have modeled the wave response of the ice shelf and sub-shelf ocean cavity to a surface gravity wave that is incident from open water. This was done using a depth-resolved 2D vertical cross-section model, accounting for full elastodynamics of the ice shelf, in contrast to most prior work that utilizes a bending plate model for the shelf. We extract frequency-dependent reflection and transmission coefficients from our time-domain simulation results, in particular focusing on the amplitude of transmitted flexural gravity and extensional Lamb waves. The incident waves cause pressure changes in the water column at the ice shelf edge produce a time-varying horizontal force on the submerged portion of the ice shelf edge, which excites extensional Lamb waves. A quantitative version of this theory shows excellent agreement with our simulation results.

Our model also provides a prediction of the horizontal and vertical displacements of the ice shelf surface, which are primarily controlled by extensional Lamb waves and flexural gravity waves, respectively. The vertical is predicted to exceed the horizontal at frequencies greater than $\sim$0.001 Hz, which is not seen in seismic data from the Ross Ice Shelf (Bromirski et al., 2017; Chen et al., 2018). We attribute this discrepancy to the expression of tilt from flexural gravity waves on the horizontal seismometer components, which our model predicts will be larger than extensional Lamb wave horizontal displacements at frequencies in the infragravity wave band and lower.

Future extensions of this work are required to explore more realistic geometries, finite-length ice shelves and interaction with grounded ice, and the extension from 2D to 3D with obliquely incident waves. Nonetheless, our work provides an important advance in understanding the wave response of ice shelves to incident ocean waves, a problem receiving growing attention due to the possible role of wave-induced stresses in fracture and calving.

# Acknowledgements

This work was supported by the National Science Foundation (OPP-1744759). We thank Peter Bromirski for many useful discussions of the Ross Ice Shelf data and Brad Lipovsky for pointing out the possible importance of tilt.

L.S.A. was supported by National Science Foundation Graduate Research Fellowship DGE-1656518, Stanford's Enhancing Diversity in Graduate Education (EDGE) Doctoral Fellowship Program and Diversifying Academia, and Recruiting Excellence (DARE) Doctoral Fellowship Program.

J.E.M. was supported by National Science Foundation DGE-1852022 through Stanford's Summer Undergraduate Research in Geoscience and Engineering (SURGE) Program.

# Data and code availability

Numerical simulations were performed using FDMAP (`https://bitbucket.org/ericmdunham/fdmap`). Simulation input files are results are available at DOI:10.25740/qy001dt7463 (`https://purl.stanford.edu/qy001dt7463`).

# References

Aki, K. and Richards, P. *Quantitative Seismology*. Geology Seismology. University Science Books, 2002.

Aster, R. C., Lipovsky, B. P., Cole, H. M., Bromirski, P. D., Gerstoft, P., Nyblade, A., Wiens, D. A., and Stephen, R. Swell-triggered seismicity at the near-front damage zone of the Ross Ice Shelf. *Seismological Research Letters*, 92(5):2768–2792, 2021.

Banwell, A. F., MacAyeal, D. R., and Sergienko, O. V. Breakup of the Larsen B Ice Shelf triggered by chain reaction drainage of supraglacial lakes. *Geophysical Research Letters*, 40(22):5872–5876, 2013.

Banwell, A. F., Willis, I. C., Macdonald, G. J., Goodsell, B., Mayer, D. P., Powell, A., and Macayeal, D. R. Calving and rifting on the McMurdo ice shelf, Antarctica. *Annals of Glaciology*, 58(75pt1):78–87, 2017.

Biot, M. A. The interaction of Rayleigh and Stoneley waves in the ocean bottom. *Bulletin of the Seismological Society of America*, 42(1): 81–93, 1952.

Bromirski, P. D., Sergienko, O. V., and MacAyeal, D. R. Transoceanic infragravity waves impacting Antarctic ice shelves. *Geophysical Research Letters*, 37(2), 2010.

Bromirski, P. D., Chen, Z., Stephen, R. A., Gerstoft, P., Arcas, D., Diez, A., Aster, R. C., Wiens, D. A., and Nyblade, A. Tsunami and infragravity waves impacting Antarctic ice shelves. *Journal of Geophysical Research: Oceans*, 122(7):5786–5801, 2017.

Bromwich, D. H. and Nicolas, J. P. Ice-sheet uncertainty. *Nature Geoscience*, 3(9):596–597, 2010.

Brunt, K. M., Okal, E. A., and MacAYEAL, D. R. Antarctic ice-shelf calving triggered by the Honshu (Japan) earthquake and tsunami, March 2011. *Journal of Glaciology*, 57(205):785–788, 2011.

Chen, Z., Bromirski, P. D., Gerstoft, P., Stephen, R. A., Wiens, D. A., Aster, R. C., and Nyblade, A. A. Ocean-excited plate waves in the ross and Pine Island Glacier ice shelves. *Journal of Glaciology*, 64(247):730–744, 2018.

Chen, Z., Bromirski, P., Gerstoft, P., Stephen, R., Lee, W. S., Yun, S., Olinger, S., Aster, R., Wiens, D., and Nyblade, A. Ross Ice Shelf icequakes associated with ocean gravity wave activity. *Geophysical Research Letters*, 46(15):8893–8902, 2019.

Dingemans, M. W. *Water wave propagation over uneven bottoms: Linear wave propagation*, volume 13. World Scientific, 1997.

Dunham, E. M., Belanger, D., Cong, L., and Kozdon, J. E. Earthquake ruptures with strongly rate-weakening friction and off-fault plasticity, Part 1: Planar faults. *Bulletin of the Seismological Society of America*, 101(5):2296–2307, 2011.

Dupont, T. and Alley, R. Assessment of the importance of ice-shelf buttressing to ice-sheet flow. *Geophysical Research Letters*, 32(4), 2005.

Ewing, M. and Crary, A. Propagation of elastic waves in ice. Part ii. *Physics*, 5(7):181–184, 1934.

Fox, C. and Squire, V. A. Reflection and transmission characteristics at the edge of shore fast sea ice. *Journal of Geophysical Research: Oceans*, 95(C7):11629–11639, 1990.

Fox, C. and Squire, V. A. Coupling between the ocean and an ice shelf. *Annals of Glaciology*, 15:101–108, 1991.

Holdsworth, G. and Glynn, J. Iceberg calving from floating glaciers by a vibrating mechanism. *Nature*, 274(5670):464–466, 1978.

Ilyas, M., Meylan, M. H., Lamichhane, B., and Bennetts, L. G. Time-domain and modal response of ice shelves to wave forcing using the finite element method. *Journal of Fluids and Structures*, 80:113–131, 2018.

Kalyanaraman, B., Bennetts, L. G., Lamichhane, B., and Meylan, M. H. On the shallow-water limit for modelling ocean-wave induced ice-shelf vibrations. *Wave Motion*, 90:1–16, 2019.

Kalyanaraman, B., Meylan, M. H., Bennetts, L. G., and Lamichhane, B. P. A coupled fluid-elasticity model for the wave forcing of an ice-shelf. *Journal of Fluids and Structures*, 97:103074, 2020.

Kozdon, J. E., Dunham, E. M., and Nordström, J. Interaction of waves with frictional interfaces using summation-by-parts difference operators: Weak enforcement of nonlinear boundary conditions. *Journal of Scientific Computing*, 50(2):341–367, 2012.

Kozdon, J. E., Dunham, E. M., and Nordström, J. Simulation of dynamic earthquake ruptures in complex geometries using high-order finite difference methods. *Journal of Scientific Computing*, 55(1):92–124, 2013.

Kundu, P. K., Cohen, I. M., and Dowling, D. R. *Fluid Mechanics*. Academic Press, 2015.

Lamb, H. On deep-water waves. *Proceedings of the London Mathematical Society*, 2(1):371–400, 1905.

Lipovsky, B. P. Ice shelf rift propagation and the mechanics of wave-induced fracture. *Journal of Geophysical Research: Oceans*, 123(6): 4014–4033, 2018.

Lotto, G. C. and Dunham, E. M. High-order finite difference modeling of tsunami generation in a compressible ocean from offshore earthquakes. *Computational Geosciences*, 19(2):327–340, 2015.

MacAyeal, D. R., Okal, E. A., Aster, R. C., Bassis, J. N., Brunt, K. M., Cathles, L. M., Drucker, R., Fricker, H. A., Kim, Y.-J., Martin, S., et al. Transoceanic wave propagation links iceberg calving margins of Antarctica with storms in tropics and Northern Hemisphere. *Geophysical Research Letters*, 33(17), 2006.

Massom, R. A., Scambos, T. A., Bennetts, L. G., Reid, P., Squire, V. A., and Stammerjohn, S. E. Antarctic ice shelf disintegration triggered by sea ice loss and ocean swell. *Nature*, 558(7710):383–389, 2018.

Mattsson, K., Dunham, E. M., and Werpers, J. Simulation of acoustic and flexural-gravity waves in ice-covered oceans. *Journal of Computational Physics*, 373:230–252, 2018.

Meylan, M. H., Ilyas, M., Lamichhane, B. P., and Bennetts, L. G. Swell-induced flexural vibrations of a thickening ice shelf over a shoaling seabed. *Proceedings of the Royal Society A*, 477(2254):20210173, 2021.

Miles, J. W. Surface-wave scattering matrix for a shelf. *Journal of Fluid Mechanics*, 28(4):755–767, 1967.

Newman, J. Propagation of water waves over an infinite step. *Journal of Fluid Mechanics*, 23(2):399–415, 1965.

Olinger, S., Lipovsky, B., Wiens, D., Aster, R., Bromirski, P., Chen, Z., Gerstoft, P., Nyblade, A., and Stephen, R. Tidal and thermal stresses drive seismicity along a major Ross Ice Shelf rift. *Geophysical Research Letters*, 46(12):6644–6652, 2019.

Olinger, S., Lipovsky, B. P., Denolle, M., and Crowell, B. W. Tracking the cracking: a holistic analysis of rapid ice shelf fracture using seismology, geodesy, and satellite imagery on the Pine Island Glacier ice shelf, West Antarctica. *Geophysical Research Letters*, page e2021GL097604, 2022.

Paolo, F. S., Fricker, H. A., and Padman, L. Volume loss from Antarctic ice shelves is accelerating. *Science*, 348(6232):327–331, 2015.

Press, F. and Ewing, M. Propagation of elastic waves in a floating ice sheet. *Eos, Transactions American Geophysical Union*, 32(5):673–678, 1951.

Pritchard, H., Ligtenberg, S. R., Fricker, H. A., Vaughan, D. G., van den Broeke, M. R., and Padman, L. Antarctic ice-sheet loss driven by basal melting of ice shelves. *Nature*, 484(7395):502–505, 2012.

Rignot, E., Jacobs, S., Mouginot, J., and Scheuchl, B. Ice-shelf melting around Antarctica. *Science*, 341(6143):266–270, 2013.

Rodgers, P. The response of the horizontal pendulum seismometer to Rayleigh and Love waves, tilt, and free oscillations of the Earth. *Bulletin of the Seismological Society of America*, 58(5):1385–1406, 1968.

Sells, C. L. The effect of a sudden change of shape of the bottom of a slightly compressible ocean. *Philosophical Transactions of the Royal Society of London. Series A, Mathematical and Physical Sciences*, 258(1092):495–528, 1965.

Sergienko, O. V. Elastic response of floating glacier ice to impact of long-period ocean waves. *Journal of Geophysical Research: Earth Surface*,

115(F4), 2010.

Sergienko, O. V. Normal modes of a coupled ice-shelf/sub-ice-shelf cavity system. *Journal of Glaciology*, 59(213):76–80, 2013.

Sergienko, O. V. Behavior of flexural gravity waves on ice shelves: Application to the Ross Ice Shelf. *Journal of Geophysical Research: Oceans*, 122(8):6147–6164, 2017.

Squire, V. A. Of ocean waves and sea-ice revisited. *Cold Regions Science and Technology*, 49(2):110–133, 2007.

Squire, V. A., Dugan, J. P., Wadhams, P., Rottier, P. J., and Liu, A. K. Of ocean waves and sea ice. *Annual Review of Fluid Mechanics*, 27(1): 115–168, 1995.

Tanimoto, T. and Wang, J. Low-frequency seismic noise characteristics from the analysis of co-located seismic and pressure data. *Journal of Geophysical Research: Solid Earth*, 123(7):5853–5885, 2018.

Tazhimbetov, N., Almquist, M., Werpers, J., and Dunham, E. Simulation of flexural-gravity wave propagation for elastic plates in shallow water using energy-stable finite difference method with weakly enforced boundary and interface conditions. *Available at SSRN 4147169*, 2022.

Timoshenko, S. P. and Goodier, J. N. *Theory of Elasticity*. McGraw Hill, 1970.

Walker, R., Dupont, T., Parizek, B., and Alley, R. Effects of basal-melting distribution on the retreat of ice-shelf grounding lines. *Geophysical Research Letters*, 35(17), 2008.

Yamamoto, T. Gravity waves and acoustic waves generated by submarine earthquakes. *International Journal of Soil Dynamics and Earthquake Engineering*, 1(2):75–82, 1982.

# A Wave modes in ice-covered water

In this appendix, we seek $e^{i(kx-\omega t)}$ solutions for an elastic ice shelf over an acoustic ocean with gravity. This problem was solved by Press and Ewing (1951) for infinitely deep water and by Lipovsky (2018) for finite depth (but incompressible) water. For simplicity we do not use the hat notation for frequency-domain fields that is used in the main text. The solution is developed by solving for the response in the ice and water, separately, to an imposed pressure $P$ on the side bounding the ice-water interface. For the ice, this means $-\sigma_{zz} = P$, and for the water, this means $p - \rho g\eta = P$. This response includes the vertical velocity $v_z$ at the same location, which defines the impedances of the ice and water layers, $Z_i$ and $Z_w$, defined as $P/v_z$. Enforcing interface conditions (12)-(14) is equivalent to matching impedance: $Z_w = Z_i$, a convenient procedure used by (Biot, 1952) for a related problem. For notational convenience, the $e^{i(kx-\omega t)}$ term is implied, and we denote the water depth as $H$ and ice thickness as $2h$. Furthermore, we place $z = 0$ at different locations when deriving the water and ice response to simplify the solution.

## A.1 Impedance of acoustic ocean with gravity

The general solution in the water, with $z = 0$ being the water surface, is (Kundu et al., 2015)

$$p = A\sinh(\kappa z) + B\cosh(\kappa z), \tag{69}$$

$$v_x = \frac{k}{\rho_w \omega}\left[A\sinh(\kappa z) + B\cosh(\kappa z)\right], \tag{70}$$

$$v_z = \frac{\kappa}{i\rho_w \omega}\left[A\cosh(\kappa z) + B\sinh(\kappa z)\right], \tag{71}$$

$$\eta = A\frac{\kappa}{\rho_w \omega^2}, \tag{72}$$

where $\kappa = \sqrt{k^2 - \omega^2/c_0^2}$ and the coefficients $A$ and $B$ are to be determined. Setting $v_z = 0$ on $z = -H$ gives

$$\begin{aligned} &A\cosh(\kappa H) \\ &- B\sinh(\kappa H) = 0. \end{aligned} \tag{73}$$

Next we enforce $p - \rho_w g\eta = P$ on $z = 0$ to obtain

$$-\frac{g\kappa}{\omega^2}A + B = P. \tag{74}$$

It follows that

$$A = \frac{\sinh(\kappa H)}{D_0}P, \tag{75}$$

$$B = \frac{\cosh(\kappa H)}{D_0}P, \tag{76}$$

$$D_0 = \cosh(\kappa H) - \frac{g\kappa}{\omega^2}\sinh(\kappa H), \tag{77}$$

where $D_0 = 0$ is the dispersion relation for wave modes in an ocean with a free surface on top. The impedance is

$$Z_w = \frac{i\omega\rho_w D_0}{\kappa\sinh(\kappa H)}. \tag{78}$$

## A.2 Impedance of elastic ice shelf

Next we solve for the response of an elastic ice shelf of thickness $2h$. It is convenient to set $z = 0$ along the centerline with boundary conditions enforced at $z = \pm h$. The displacements and traction components of stress are

$$u_x = k\left(A_1 e^{-pz} + A_2 e^{pz}\right) + iq\left(B_1 e^{-qz} - B_2 e^{qz}\right), \tag{79}$$
$$u_z = ip\left(A_1 e^{-pz} - A_2 e^{pz}\right) - k\left(B_1 e^{-qz} + B_2 e^{qz}\right), \tag{80}$$
$$\sigma_{xz}/\mu = -2kp\left(A_1 e^{-pz} - A_2 e^{pz}\right) - i\left(k^2+q^2\right)\left(B_1 e^{-qz} + B_2 e^{qz}\right), \tag{81}$$
$$\sigma_{zz}/\mu = -i\left(k^2+q^2\right)\left(A_1 e^{-pz} + A_2 e^{pz}\right) + 2kq\left(B_1 e^{-qz} - B_2 e^{qz}\right), \tag{82}$$

for coefficients $A_i$, $B_i$ and

$$p = \sqrt{k^2 - \omega^2/c_p^2} \tag{83}$$
$$q = \sqrt{k^2 - \omega^2/c_s^2}. \tag{84}$$

Note that symmetric modes will have $A_1 - A_2 = 0$ and $B_1 + B_2 = 0$, whereas antisymmetric modes will have $A_1 + A_2 = 0$ and $B_1 - B_2 = 0$.

Next we enforce $\sigma_{xz} = 0$ on $z = \pm h$, $\sigma_{zz} = 0$ on $z = h$, and $\sigma_{zz} = -P$ on $z = -h$:

$$-2kp\left(A_1 e^{-ph} - A_2 e^{ph}\right) - i\left(k^2+q^2\right)\left(B_1 e^{-qh} + B_2 e^{qh}\right) = 0, \tag{85}$$
$$-2kp\left(A_1 e^{ph} - A_2 e^{-ph}\right) - i\left(k^2+q^2\right)\left(B_1 e^{qh} + B_2 e^{-qh}\right) = 0, \tag{86}$$
$$-i\left(k^2+q^2\right)\left(A_1 e^{-ph} + A_2 e^{ph}\right) + 2kq\left(B_1 e^{-qh} - B_2 e^{qh}\right) = 0, \tag{87}$$
$$-i\left(k^2+q^2\right)\left(A_1 e^{ph} + A_2 e^{-ph}\right) + 2kq\left(B_1 e^{qh} - B_2 e^{-qh}\right) = -\frac{P}{\mu}. \tag{88}$$

Then form linear combinations of the resulting equations to highlight excitation of symmetric and antisymmetric modes. Symmetric modes are determined by

$$-2kp\sinh(ph)(A_1 + A_2) - i\left(k^2+q^2\right)\sinh(qh)(B_1 - B_2) = 0, \tag{89}$$
$$-i\left(k^2+q^2\right)\cosh(ph)(A_1 + A_2) + 2kq\cosh(qh)(B_1 - B_2) = -\frac{P}{2\mu}, \tag{90}$$

and antisymmetric modes by

$$-2kp\cosh(ph)(A_1 - A_2) - i\left(k^2+q^2\right)\cosh(qh)(B_1 + B_2) = 0, \tag{91}$$
$$-i\left(k^2+q^2\right)\sinh(ph)(A_1 - A_2) + 2kq\sinh(qh)(B_1 + B_2) = -\frac{P}{2\mu}. \tag{92}$$

The determinants of the coefficient matrices provide the dispersion relations for symmetric ($D_S = 0$) and antisymmetric ($D_A = 0$) modes of an elastic layer bounded by free surfaces:

$$D_S = 4k^2pq\sinh(ph)\cosh(qh) - \left(k^2+q^2\right)^2\cosh(ph)\sinh(qh), \tag{93}$$
$$D_A = 4k^2pq\cosh(ph)\sinh(qh) - \left(k^2+q^2\right)^2\sinh(ph)\cosh(qh). \tag{94}$$

The dispersion relations $D_S = 0$ and $D_A = 0$ are more often written as **?**e.g.,>lamb1917waves, achenbach1973wave, achenbach2003reciprocity

$$\frac{\tanh(qh)}{\tanh(ph)} = \frac{4k^2pq}{\left(k^2+q^2\right)^2} \quad \text{(symmetric)}, \tag{95}$$
$$\frac{\tanh(qh)}{\tanh(ph)} = \frac{\left(k^2+q^2\right)^2}{4k^2pq} \quad \text{(antisymmetric)}. \tag{96}$$

The coefficients are given by

$$A_1 + A_2 = \frac{i\left(k^2+q^2\right)\sinh(qh)}{D_S}\frac{P}{2\mu}, \tag{97}$$
$$B_1 - B_2 = -\frac{2kp\sinh(ph)}{D_S}\frac{P}{2\mu}, \tag{98}$$
$$A_1 - A_2 = \frac{i\left(k^2+q^2\right)\cosh(qh)}{D_A}\frac{P}{2\mu}, \tag{99}$$
$$B_1 + B_2 = -\frac{2kp\cosh(ph)}{D_A}\frac{P}{2\mu}, \tag{100}$$

and hence,

$$A_1 = i\left(k^2+q^2\right)\left[\frac{\sinh(qh)}{D_S}+\frac{\cosh(qh)}{D_A}\right]\frac{P}{4\mu}, \tag{101}$$

$$A_2 = i\left(k^2+q^2\right)\left[\frac{\sinh(qh)}{D_S}-\frac{\cosh(qh)}{D_A}\right]\frac{P}{4\mu}, \tag{102}$$

$$B_1 = -2kp\left[\frac{\sinh(ph)}{D_S}+\frac{\cosh(ph)}{D_A}\right]\frac{P}{4\mu}, \tag{103}$$

$$B_2 = -2kp\left[-\frac{\sinh(ph)}{D_S}+\frac{\cosh(ph)}{D_A}\right]\frac{P}{4\mu}. \tag{104}$$

Next we calculate impedance of the ice as $Z_i = P/v_z$, where $v_z = -i\omega u_z$ is evaluated at $z = -h$:

$$Z_i = \frac{2i\rho_i c_s^4}{\omega^3 pF}, \tag{105}$$

$$F = \frac{\sinh(ph)\sinh(qh)}{D_S}+\frac{\cosh(ph)\cosh(qh)}{D_A}. \tag{106}$$

## A.3 Dispersion relation for coupled ice-water system

The dispersion relation for the coupled system is obtained by matching impedance, $Z_w = Z_i$, yielding

$$\frac{\omega\rho_w D_0}{\kappa\sinh(\kappa H)} = \frac{2\rho_i c_s^4}{\omega^3 pF}. \tag{107}$$